



UPPSALA
UNIVERSITET

DiVA 

<http://uu.diva-portal.org>

This is an author produced version of a paper published in *Solar Energy Materials and Solar Cells*. This paper has been peer-reviewed but does not include the final publisher proof-corrections or journal pagination.

Citation for the published paper:

Schleussner, Sebastian et. al.

"Effect of gallium grading in Cu(In,Ga)Se₂ solar-cell absorbers produced by multi-stage coevaporation"

Solar Energy Materials and Solar Cells, 2011, Vol. 95, Issue 2: 721-726

[URL: http://dx.doi.org/10.1016/j.solmat.2010.10.011](http://dx.doi.org/10.1016/j.solmat.2010.10.011)

Access to the published version may require subscription.



Effect of gallium grading in Cu(InGa)Se₂ solar-cell absorbers produced by multi-stage coevaporation

Sebastian Schleussner^{a,*}, Uwe Zimmermann^a, Timo Wätjen^{a,b}, Klaus Leifer^b, Marika Edoff^a

^a*Solid State Electronics, Uppsala University, P.O. Box 534, SE-751 21 Uppsala, Sweden.
Tel.: +46184713113; fax: +4618555095.*

^b*Electron Microscopy and Nanoengineering, Uppsala University, P.O. Box 534, SE-751 21 Uppsala, Sweden.*

Abstract

We investigate Cu(InGa)Se₂ thin films grown in multi-stage coevaporation processes and solar cells fabricated from such absorbers. Despite some interdiffusion during film growth, Ga/(Ga+In) gradients defined via evaporation-profile variations in the process are to a good part retained in the finished film. This indicates that the bandgap can be engineered in this type of process by varying the evaporation profiles, and consequently also that unintended profile variations should be noted and avoided. With front-side gradients the topmost part of many grains seems to be affected by a higher density of lattice defects due to the strong change of gallium content under copper-poor growth conditions. Electrically, both back-side gradients and moderate front-side gradients are shown to yield an improvement of device efficiency. If a front-side gradient is too wide, though, it causes strong voltage-dependent collection and the fill factor is severely reduced.

This is the author's version of a work that was accepted for publication in Solar Energy Materials and Solar Cells. Changes resulting from the publishing process, such as editing, corrections and structural formatting may not be reflected in this document. A definitive version was subsequently published in Solar Energy Materials and Solar Cells 95 (2011) pp. 721–726, doi: 10.1016/j.solmat.2010.10.011.

Keywords: CIGS, Coevaporation, Multi-stage process, Three-stage process, Gradients

1. Introduction

The absorbers of the latest record-efficiency solar-cell devices based on Cu(InGa)Se₂ (CIGS) were prepared by three- or multi-stage evaporation processes [1, 2]. This is at least in part attributed to the fact that this process gives rise to a spontaneous ‘notch’ grading of the gallium content $GGI := [Ga]/[In + Ga]$ [3], for which Gabor *et al.* offer a growth model [4]. By changing the gallium content from $x = 0$ to $x = 1$, the bandgap of CIGS can be adjusted approximately from 1.0 eV to 1.7 eV, with the bandgap variation affecting almost exclusively the position of the conduction-band edge (see for instance [5]). Thus, the ‘notch’ structure is equivalent to a low-bandgap semiconductor layer being sandwiched between two layers of higher bandgap that was projected by modelling to be optimal for device performance [6].

As the Ga content decreases from the rear towards the middle of the absorber it induces a back-surface field in the conduction band [7, 8], which causes electrons to drift away from the rear contact and thereby reduces the risk of recombination at the contact. The back-surface grading thus can improve the open-circuit voltage V_{OC} . It may also marginally increase the short-circuit current density J_{SC} thanks to an im-

provement of the carrier-collection efficiency close to the rear contact.

The potential benefit of front-surface grading as represented by the second part of the notch structure is the decoupling of photogeneration and carrier recombination [5]. As Dullweber *et al.* [9] have found, the optical bandgap determining J_{SC} in frontside-graded CIGS corresponds well to the minimum bandgap $E_{g,min}$, while interface recombination and thus V_{OC} depend on the bandgap in the space-charge region, $E_{g,SCR}$. At the same time, it has to be kept in mind that too wide or too strong Ga gradients may act as barriers for electrons on their way to the junction. This would cause poor and voltage-dependent photocurrent collection [10].

In this work we show that intentional Ga grading added to the spontaneous gradients are retained to a good degree in CIGS absorbers grown by multi-stage co-evaporation. We also examine the influence of various gradings on the performance of solar-cell devices prepared from those absorbers and present some guidelines for the design of high-efficiency CIGS solar cells.

*Corresponding author.

Email address: sebastian.schleussner@angstrom.uu.se
(Sebastian Schleussner)

2. Experimental

2.1. CIGS and device fabrication

The solar-cell devices were fabricated on 1-mm thick sheets of soda-lime glass with molybdenum back contacts of 300 nm thickness deposited by DC magnetron sputtering, in accordance with our group's baseline procedure [11].

The CIGS layers were deposited by co-evaporation of the elements Cu, In and Ga from fast-acting open boat sources in a Se atmosphere maintained from a crucible source kept at a constant temperature. The metal rates were controlled using mass-spectrometer feedback. The Se temperature was chosen such that it was safe to assume that the Se evaporation rate was several times higher than that required for the formation of stoichiometric $\text{Cu}(\text{InGa})\text{Se}_2$ at all times during the process. The process was carried out in a vacuum chamber pumped to a pressure of below 2×10^{-6} mbar holding three $5 \times 5 \text{ cm}^2$ substrates per run. Further details on the CIGS processes are given in Section 2.3 below.

Device completion once more followed our group's baseline procedure, comprising a 50 nm CdS buffer layer grown by chemical bath deposition, an RF-sputtered 50 nm layer of intrinsic ZnO, a DC-sputtered 300 nm film of Al-doped ZnO as a conductive window layer, a current-collecting Ni-Al-Ni grid and mechanical scribing to define separated 0.5 cm^2 cells.

2.2. Analyses

The composition of the CIGS films was determined by X-ray fluorescence (XRF) performed in a *Spectro X-lab 2000* and the thickness was measured with a *Dektak V 200-Si* profilometer. The XRF count rates were scaled with a linear model to yield atomic percentages. Elemental depth profiles of absorbers capped with the CdS buffer layer were analysed by means of secondary ion mass spectrometry (SIMS) in a *Cameca IMS 4f* system, using Cs^+ ions at 9 kV acceleration voltage.

The symbols $\text{GGI} := [\text{Ga}]/[\text{In} + \text{Ga}]$ and $\text{CGI} := [\text{Cu}]/[\text{In} + \text{Ga}]$ are used in the following to denote the atomic ratios of gallium versus both group-III elements and copper versus the group-III elements, respectively; in particular, GGI^* and CGI^* stand for the *final*, average gallium and copper contents as measured by XRF.

The recipe and SIMS graphs are scaled such that for every element, the average of the profile matches the corresponding content according to the XRF data. For the recipe graphs, we assume a constant sticking coefficient for each of the evaporated metals. The x-axes of the SIMS depths profiles are calibrated with the measured film thickness, assuming a constant sputter rate.

Transmission-electron microscopy (TEM) analyses were performed on several samples in a *FEI Tecnai F30 ST* microscope operating at 300 kV; also electron-microdiffraction patterns were viewed here.

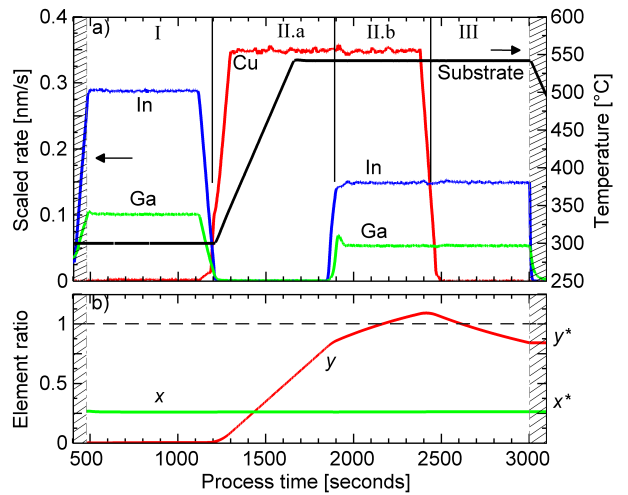


Figure 1: a) Evaporation rates of the metals Cu, In and Ga and substrate temperature of the ungraded reference process **A** as a function of process time. The rates are scaled data from the in-situ mass spectrometer. b) Integrated composition in terms of the ratios $\text{GGI} = [\text{Ga}]/[\text{In} + \text{Ga}]$ and $\text{CGI} = [\text{Cu}]/[\text{In} + \text{Ga}]$.

Energy-dispersive X-ray analysis (EDX) line scans of the samples were recorded while in scanning transmission-electron microscope (STEM) mode. In contrast to the SIMS data, the EDX spectra were translated into composition data based on a standardless quantification only and not further calibrated with XRF results. This is the reason for the discrepancy between the two methods that is seen in Figure 3 below.

Cells were characterized by current vs. voltage (IV) measurements with illumination from an ELH lamp. The external quantum efficiency (QE) was determined under ambient light, using chopped monochromatic light that was scanned through the wavelength interval of 360 nm to 1200 nm in 10-nm steps.

2.3. CIGS recipe specifics

Figure 1 a) shows the rate and temperature profiles of the reference CIGS recipe which contains no gallium grading in the evaporation profiles. Our CIGS process is based on the three-stage process [3], where the evaporation of In, Ga and Se on a relatively cool substrate ('stage I') is followed by the evaporation of Cu and Se at a high temperature ('stage II'), which after a transition of the composition to Cu-richness is capped by further evaporation of the group-III elements In and Ga together with Se ('stage III') to make the final film Cu-poor. Differing from the most basic three-stage processes, our recipe features an overlap of the stages II and III. This emulates the configuration in an inline system where the low-temperature stage I is located in its own segment of the vacuum system but stages II and III are closer together. Because of the overlap, we refer to our process as a *multi-stage* process, with the basic

phases denoted as marked in the figure. We divide stage *II* further into the Cu-only stage *II.a*, and stage *II.b* where both Cu and the group-III elements are evaporated. The durations of the various stages are listed in Table 1. We use box-like evaporation profiles in order to make the definition of gradings straightforward. Another characteristic of our recipe is the relatively long third stage. This allows for a larger process window in our rate-controlled system, which does not use end-point detection [12]. The substrate was kept at a temperature of 300 °C during the first stage. During the second stage this temperature was ramped up to 540 °C and it was then held at that value until the end of the evaporation. After that, the heater was turned off and the samples left to cool in the vacuum.

Figure 1 b) displays the development of the *integral* of the film composition in the reference process over time, as calculated from the final composition and the given evaporation profiles. These values can be thought of as estimations of the result of XRF measurements at the corresponding points in time. Note the constant level of the gallium-to-group-III ratio GGI for evaporation in this recipe, and how the copper-to-group-III ratio CGI moves to a value above unity and then back. We compare this reference recipe, which has given rise to sample **A**, with three recipes where the evaporated ratio GGI is graded, yielding the samples **B**, **C** and **D** listed in Table 1. The general recipe variant, which has gallium grading both at the back and at the front, is represented in Figure 2 by sample **C**. In Figure 2 a) the steps in the gallium and indium evaporation profiles are clearly visible in the beginning and at the end of the evaporation. The resulting *momentary* values $\text{GGI}_{\text{momentary}}$ of the ratio $[\text{Ga}]/[\text{In} + \text{Ga}]$ at the growth surface, calculated from the evaporation rates, are plotted in Figure 2 b) together with the integrals calculated from the growing film as above. We denote the new partial stage supplying the back-side grading as stage *I.a*, and the one supplying the front-side grading as stage *III.b*. The durations used for these stages in the considered processes are given in Table 1, with a dash ‘-’ meaning that the respective grading was not applied. The partial stages *I.b* and *III.a* were shortened correspondingly so that the

Table 1: Process parameters for the samples discussed in this paper. Thickness, GGI* and CGI* denote the actually obtained absorber thickness and average composition; The times t_N refer to the durations of the respective stages *N*. Dashes ‘-’ in these columns mean that the corresponding grading was not applied.

Sample	thickness [μm]	GGI*	CGI*	t_I [s]	$t_{II.a}$ [s]	$t_{II.b}$ [s]	t_{III} [s]	$t_{I.a}$ [s]	$t_{III.b}$ [s]
A	1.71	0.26	0.84	720	690	570	540	-	-
B	1.63	0.28	0.85	720	690	570	540	180	-
C	1.70	0.29	0.86	720	690	570	540	180	140
D	1.58	0.32	0.89	720	690	570	540	180	300

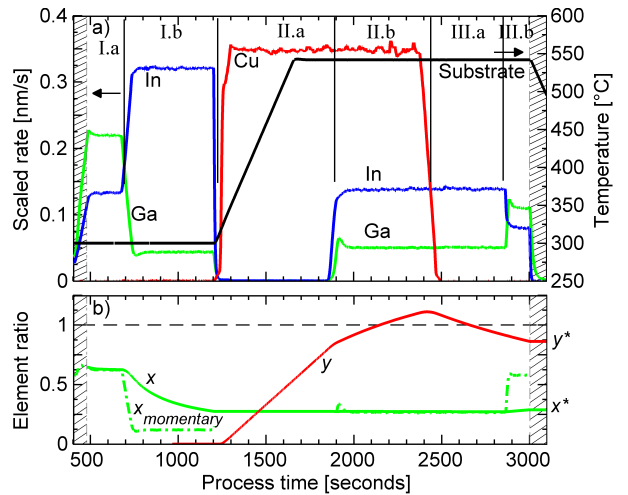


Figure 2: a) Evaporation rates and substrate temperature of process **C** as a representative of the recipes featuring graded evaporation profiles. b) Integrated composition in terms of the ratios GGI and CGI (solid lines), and the momentary GGI ratio (dash-dotted line).

process duration of the reference was maintained in all cases.

As seen in Figure 2 b), the Ga content was set to $\text{GGI} = 0.6$ in stages *I.a* and *III.b*. In order to keep the average value of GGI at the same level as in the reference, GGI was reduced to approximately 0.12 in stage *I.b* if the back-side grading was applied.

3. Results and Discussion

3.1. Material properties

Figure 3 shows the SIMS depth profiles of all considered samples. The data for the reference sample **A** show that the process without intentional grading creates a soft intrinsic double gallium gradient, with a minimum of the Ga content GGI situated in the middle of the film and with rising gallium contents towards the front and back surfaces. This profile corresponds to the ‘notch’ structure typically observed in absorbers fabricated by three-stage processes, see for instance [3]. Gabor *et al.* [4] offer a model of the growth kinetics based on the view that preferential out-diffusion of In into Cu-rich areas lowers the strain energy of the film because In has a larger atomic radius than Ga.

In contrast to this it is obvious from the data of sample **B** that a significant additional gradient has developed here due to the variation of the evaporation rates between stages *I.a* and *I.b*. According to the SIMS profile the concentration gradients in the film, compared to the as-deposited steps, are smoothed with reduced extremes. In considering SIMS data, one has to keep in mind that the depth profiles tend to be affected by matrix effects and cascade mixing [13]. On the other hand, the TEM-EDX concentration profile reproduces a very similar shape, as demonstrated for sample **B** in the figure. It is thus

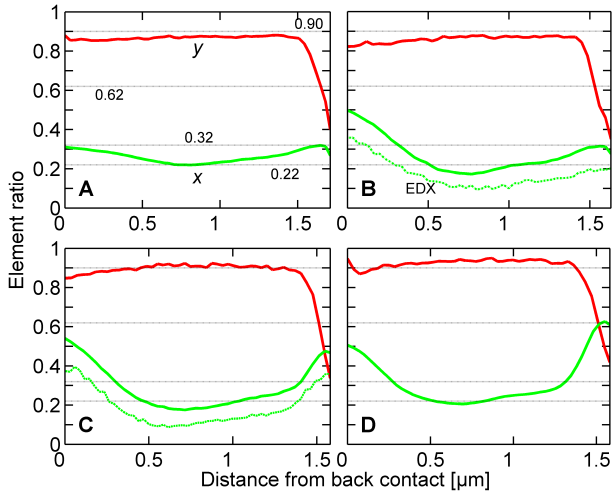


Figure 3: SIMS profiles of all samples in terms of the ratios $GGI = [Ga]/[In + Ga]$ and $CGI = [Cu]/[In + Ga]$. For samples **B** and **C**, the GGI profiles according to TEM-EDX are shown as well (dash-dotted lines). The deviation in absolute values can be explained by the fact that the EDX composition data were scaled according to a standardless quantification only and not calibrated with XRF as the SIMS data.

safe to assume that the observed profile smoothening is indeed largely due to interdiffusion during the growth process. As noted in the last paragraph of Section 2.3, the average gallium content of the film in stage *I* is the same in all samples as in the reference, so we can exclude the possibility that the difference in the gradients depends on varying average composition.

In sample **C**, the rates were not only altered in stage *I.a* but also in stage *III.b* in order to enhance the gallium gradient at the front, evaporating with a Ga content $x = 0.6$ for 140 s. Again, while diffusion has smoothened the original sharp step, a considerable part of the additional grading is retained, with the top reaching an GGI value of about 0.45, similar to the corresponding gradient at the back.

Finally, the gallium-rich stage *III.b* in sample **D** has lasted 300 s. In this case, it seems that the additional Ga affects mainly the height of the gradient rather than its extent. According to the SIMS profile, the topmost 100 nm of the Ga-rich layer maintains largely the evaporated Ga content, while the thickness of the layer is only somewhat larger than that of sample **C**.

Figure 4 shows the TEM cross-section image of a part of sample **C**. The image is representative for the samples from this series, demonstrating that our process yields large CIGS grains of around $1 \mu\text{m}$ edge width, some of which span the entire thickness of the film. As mentioned above, EDX line scans show largely the same gradients as the SIMS profiles do, and this indicates that compositions as diverse as these can well exist within one grain. A noteworthy feature in Figure 4 is the change of appearance of the topmost part of the CIGS layer. This part seems

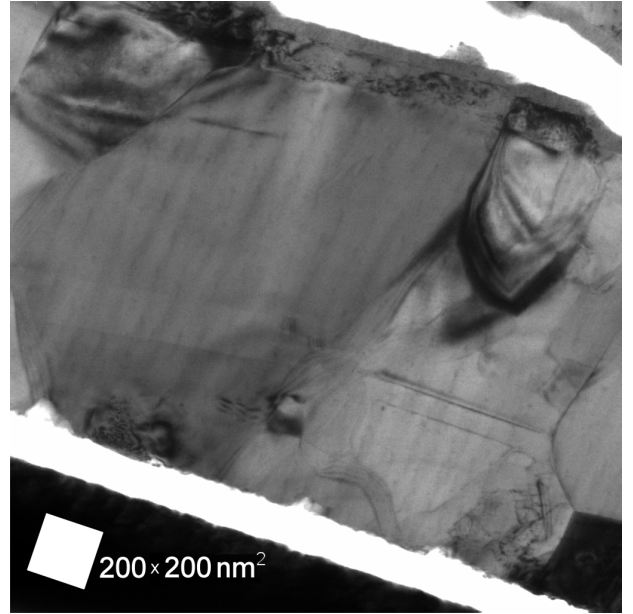


Figure 4: TEM bright-field cross-section image of sample **C**, which has gradients back and front, demonstrating the presence of large grains with an interfacial region as well as of some smaller ones. The substrate with the Mo back contact is below (separation occurred during TEM-sample preparation), the CdS buffer layer on top.

to be rich in structural defects, while the route of its onset and that of the grain boundaries suggest that it is still a particular region of the large grain rather than a separate layer of one or several grains. At circa 100 nm thickness, this region is comparable to the part of the film grown after the transition of the average composition to Cu poverty, which in SIMS and EDX also displays a drop in Cu content (cf. Figure 3). In contrast, a corresponding region is hardly, if at all, discernible in TEM images taken of sample **B**, which does not have intentional Ga grading at the front. Taken together, these observations indicate that the structural change is caused by the growth of more Ga-rich material on top of less Ga-rich material, which is structurally unfavourable [14], while under Cu-poor conditions.

In all the SIMS and EDX depth profiles in Figure 3, we also observe a strong drop of the Cu content throughout the uppermost 200 nm of the film. A corresponding increase in the Se content seen in all cases, extending from bulk values of ca. 52% to over 55%, verifies this observation. The content ultimately approaches the value $CGI = 1/3$ that would correspond to the composition of the defect compound $\text{Cu}(\text{InGa})_3\text{Se}_5$. That compound is believed to yield a favourable band lineup due to bandgap widening by lowering the valence-band edge [15]. However, the gradual transition of the copper content makes the existence of a separate phase improbable. Furthermore, like Yan *et al.* [16], electron diffraction patterns of our material showed only the reflections of the $\text{Cu}(\text{InGa})\text{Se}_2$ phase without any visible signs of the $\text{Cu}(\text{InGa})_3\text{Se}_5$ phase. We therefore view this

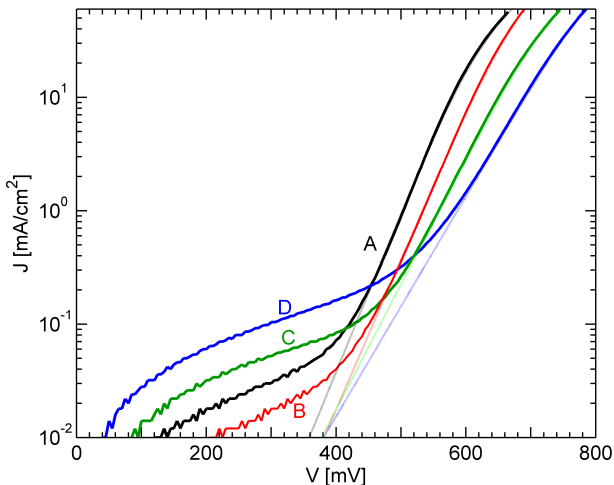


Figure 5: Semi-logarithmic plots of the dark current-voltage curves. The thin dotted lines show the results of fits according to the one-diode model, which give rise to the parameters listed in Table 2.

region of the films as a *surface-defect layer* as it is described by Rau [17], a layer that may share the electronic properties of the Cu-deficient $\text{Cu}(\text{InGa})_3\text{Se}_5$ while not forming a phase of its own.

3.2. Electrical properties

Table 2 lists the results of one-diode model fits to the dark current-voltage curves of representative solar cells of all samples, displayed in Figure 5. We note that all curves have a similar shape, showing no signs of major shunting or series resistances. With the additional back-surface gradient and the front-surface gradients of increasing thickness, the curve sections over 0.5 mA/cm^2 are progressively shifted towards higher voltages. In the case of the front-surface gradients, on the one hand, this shift can be understood as the effect of an enhanced built-in voltage due to the higher conduction-band edges in the CIGS close to the junction. On the other hand, the increase in the ideality factor from sample **A** to sample **B** and the slightly reduced short-circuit current indicate that the shift caused by the back-surface gradient is due to a relative decrease of recombination at the back contact.

Now we consider the illuminated IV curves in Figure 6 and the solar-cell parameters listed in Table 3, first comparing the characteristics of a device from

Table 2: Diode parameters extracted from one-diode model fits to dark current-voltage measurements: Saturation current density J_0 , ideality factor n_{id} , and series resistance R_S .

Sample	J_0 [mA/cm ²]	n_{id}	R_S [mΩ cm ²]
A	9.5×10^{-8}	1.20	700
B	9.0×10^{-8}	1.27	400
C	6.7×10^{-7}	1.52	500
D	2.0×10^{-6}	1.60	200

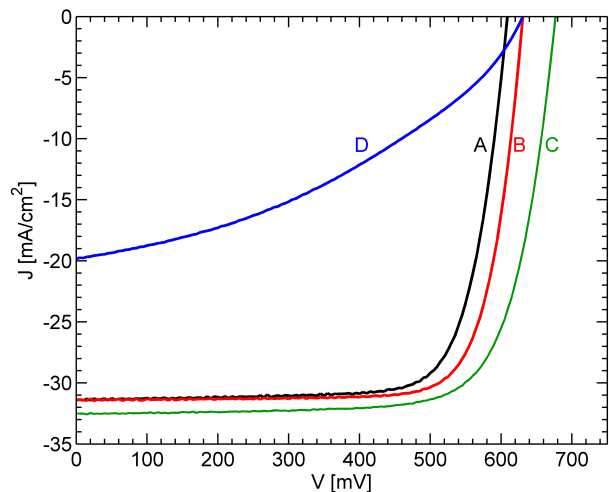


Figure 6: Current-voltage curves taken under illumination with an intensity of 1 sun at 25 °C.

the reference **A** with those of a device from sample **B**, which features the intentional gradient at the back. We see an increase in the open-circuit voltage V_{OC} corresponding to the shift in the dark diode curve above, even though somewhat smaller. This supports the view that the back-side gradient passivates the Mo-CIGS contact interface by repelling conduction-band electrons diffusing towards the rear contact, and thus reduces recombination at the contact. Moreover, as the quantum-efficiency graphs in Figure 7 show, the QE of sample **B** is slightly enhanced for long wavelengths. This is a sign of enhanced collection in the deeper regions of the CIGS film, since red and infrared light is most likely to be absorbed and thus to generate electron-hole pairs deep inside the absorber.

Adding a front-side gradient in **C** proves to improve both V_{OC} and the short-circuit current density J_{SC} , but at the expense of a small drop in the fill factor FF . The gain in open-circuit voltage is consistent with the model that the larger bandgap reduces the amount of potential recombination partners at the very p-n junction by virtue of a lower intrinsic carrier concentration n_i . Figure 7 indicates that the current gain in **C** is owed to a significant improvement of the long-wavelength quantum efficiency. We have no clear explanation for this at present; it could be the effect of a higher minority-carrier diffusion length for this particular sample.

Table 3: Solar-cell parameters extracted from electrical measurements: Short-circuit current density J_{SC} (according to QE), open-circuit voltage V_{OC} , fill factor FF , efficiency η , optical bandgap $E_{\text{g,opt}}$.

Sample	J_{SC} [mA/cm ²]	V_{OC} [mV]	FF [%]	η [%]	$E_{\text{g,opt}}$ [eV]
A	31.4	608	77	14.4	1.10
B	31.6	638	78	15.8	1.10
C	32.5	676	75	16.4	1.08
D	19.8	663	43	7.1	1.09

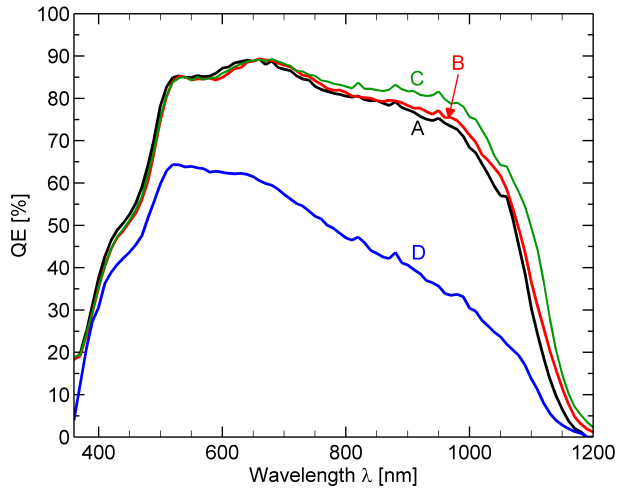


Figure 7: External quantum efficiencies of the solar-cell devices.

Lastly, sample **D** with its wider front-side gradient shows a very detrimental impact of the grading on the electrical performance in Figures 6 and 7. Since Figure 5 has proved that no significant shunting exists, it is clear that the slanted IV curve of sample **D** is the effect of voltage-dependent collection of the photocurrent, with the obvious cause being a current-blocking influence of the front-side gradient. As witnessed by the reduction of the quantum efficiency in Figure 7, and consequently the diminished J_{SC} , the gradient creates a barrier for the photocurrent even at short-circuit conditions. Indeed, the effect of voltage-dependent collection remains visible even under reverse bias up to the onset of breakdown at circa -2 V.

Generally speaking, such a barrier consists of a strong uplift of the conduction-band edge from the bulk towards the junction. Since the electric field in the space-charge region constitutes a strong drop of the energy bands [17], the existence of a barrier implies either that the gradient extends spacially beyond the space-charge region into the absorber bulk or that the bandgap widening is strong enough to cause a net elevation of the conduction-band edge within the space-charge region. In Figure 3 we have seen that the front-side gradient in sample **D** has a width of circa 300 nm. This gradient also has the highest maximum Ga content in this series, approximately $\Delta GGI = 0.3$, corresponding to a bandgap $\Delta E_g = 200$ meV larger than in the reference. The width of 300 nm is in the range of typical equilibrium depletion widths found or expected in CIGS [5]. Reverse bias widens the space-charge region and increases the band bending across it. Thus, a narrow barrier with a height of 200 meV should be easily compensated by a moderate reverse bias; but due to the weak band bending at the edge of the space-charge region, it is quite conceivable that a barrier about as wide as the zero-bias space-charge region is still effective under reverse bias. We therefore assume that the width of the gradient in sample **D** is the

primary cause for the reduced short-circuit current. Contrariwise, under forward bias, both the width and the height of the band bending in the space-charge region are reduced, diminishing the ability of the field to compensate any barrier in the conduction band. For this reason, the detrimental electrical effect seen in the low fill factor of sample **D** is certainly due to a combination of the width and the maximum height of the front-side gradient.

4. Conclusion

We have demonstrated that gallium gradients defined by means of the evaporation profiles of a multistage coevaporation CIGS process are to a good part retained in the finished film. That is true for gradients both at the front and at the back of the absorber, in spite of some interdiffusion caused by the shifts between Cu-poor and Cu-rich compositions. This indicates on the one hand that it is possible to engineer the bandgap in this type of process by means of varying the evaporation profiles. On the other hand it means that one should be aware of unintentional profile variations and be careful not to introduce large-scale variations that might give rise to detrimental gradients.

Our multistage process yields large grains, some spanning the whole film thickness. In the case of an intentional front-side gradient the appearance of the topmost part of many grains implies that the strong change of gallium content under copper-poor growth conditions causes a higher density of lattice defects.

Electrically, both grading at the back and moderate grading at the front improve the device efficiency. However, if the front-side gradient is too strong, it causes voltage-dependent collection and the fill factor is severely reduced. Thus, the process window for beneficial front-side gallium grading may be fairly small and it is not obvious if it would be practical to implement this feature in a production process.

Acknowledgements

The authors gratefully acknowledge Margareta Linnarsson for the SIMS analyses and thank Tobias Törndahl for very valuable discussions. This work was carried out as part of the LARCIS project (FP-6-019757) funded by the European Commission.

References

- [1] I. L. Repins, M. A. Contreras, B. Egaas, C. DeHart, J. Scharf, C. L. Perkins, B. To, R. Noufi, 19.9%-efficient ZnO/CdS/CuInGaSe₂ solar cell with 81.2% fill factor, *Progress in Photovoltaics: Research and Applications* 16 (2008) 235–239. doi:10.1002/pip.822.
- [2] M. Powalla, G. Voorwinden, D. Hariskos, P. Jackson, R. Kniese, Highly efficient CIS solar cells and modules made by the co-evaporation process, *Thin Solid Films* 517 (7) (2009) 2111–2114. doi:10.1016/j.tsf.2008.10.126.
- [3] M. A. Contreras, J. R. Tuttle, A. M. Gabor, A. L. Tennant, K. Ramanathan, S. E. Asher, A. Franz, J. C. Keane, L. Wang, J. Scofield, R. Noufi, High-efficiency Cu(In,Ga)Se₂-based solar cells: Processing of novel absorber structures, in: *Proceedings of the 24th IEEE Photovoltaic Specialists Conference*, 1994, pp. 68–75. URL http://www.oberlin.edu/physics/Scofield/pdf_files/pvsc-95h.pdf
- [4] A. M. Gabor, J. R. Tuttle, M. H. Bode, A. Franz, A. L. Tennant, M. A. Contreras, R. Noufi, D. G. Jensen, A. M. Hermann, Band-gap engineering in Cu(In,Ga)Se₂ thin films grown from (In,Ga)₂Se₃ precursors, *Solar Energy Materials and Solar Cells* 41–42 (1996) 247–260. doi:10.1016/0927-0248(95)00122-0.
- [5] U. Rau, H.-W. Schock, Cu(In,Ga)Se₂ solar cells, in: M. D. Archer, R. Hill (Eds.), *Clean Energy from Photovoltaics*, Imperial College Press, 2001, Ch. 7, pp. 277–345.
- [6] A. Dhingra, A. Rothwarf, Computer simulation and modeling of the graded bandgap CuInSe₂/CdS solar cell, in: *Proceedings of the 23rd IEEE Photovoltaic Specialists Conference*, 1993, pp. 475–480. doi:10.1109/pvsc.1993.347135.
- [7] M. A. Green, *Solar Cells: Operating Principles, Technology and System Applications*, Prentice-Hall, 1998.
- [8] T. Dullweber, O. Lundberg, J. Malmström, M. Bodegrd, L. Stolt, U. Rau, H.-W. Schock, J. H. Werner, Back surface band gap gradings in Cu(In,Ga)Se₂ solar cells, *Thin Solid Films* 387 (1–2) (2001) 11–13. doi:10.1016/S0040-6090(00)01726-0.
- [9] T. Dullweber, U. Rau, M. A. Contreras, R. Noufi, H.-W. Schock, Photogeneration and carrier recombination in graded gap Cu(In,Ga)Se₂ solar cells, *IEEE Transactions on Electron Devices* 47 (12) (2000) 2249–2254. doi:10.1109/16.887004.
- [10] M. Gloeckler, J. R. Sites, Band-gap grading in Cu(In,Ga)Se₂ solar cells, *Journal of Physics and Chemistry of Solids* 66 (11) (2005) 1891–1894. doi:10.1016/j.jpcs.2005.09.087.
- [11] J. Kessler, M. Bodegrd, J. Hedström, L. Stolt, Baseline Cu(In,Ga)Se₂ device production: control and statistical significance, *Solar Energy Materials and Solar Cells* 67 (1–4) (2001) 67–76. doi:10.1016/S0927-0248(00)00264-6.
- [12] J. Schldström, J. Kessler, M. Edoff, Two-stage growth of smooth Cu(In,Ga)Se₂ films using end-point detection, *Thin Solid Films* 480–481 (2005) 61–6. doi:10.1016/j.tsf.2004.11.076.
- [13] M. K. Linnarsson, B. G. Svensson, Cascade mixing in Al_xGa_{1-x}As/GaAs during sputter profiling by noble-gas ions, *Physical Review B* 60 (20) (1999) 14302–14310. doi:10.1103/PhysRevB.60.14302.
- [14] S. Seyrling, S. Bcheler, A. Chirila, J. Perrenoud, S. Wenger, T. Nakada, M. Grtzel, A. N. Tiwari, Development of multijunction thin film solar cells, in: *Proceedings of the 34th IEEE Photovoltaic Specialists Conference*, 2009, pp. 000622–000625. doi:10.1109/PVSC.2009.5411607.
- [15] D. Schmid, M. Ruckh, F. Grunwald, H.-W. Schock, Chalcopyrite/defect chalcopyrite heterojunctions on the basis of CuInSe₂, *Journal of Applied Physics* 73 (1993) 2902–2909. doi:10.1063/1.353020.
- [16] Y. Yan, K. M. Jones, J. AbuShama, M. Young, S. E. Asher, M. M. Al-Jassim, R. Noufi, Microstructure of surface layers in Cu(In,Ga)Se₂ thin films, *Applied Physics Letters* 81 (6) (2002) 1008–1010. doi:10.1063/1.1498499.
- [17] U. Rau, Electronic properties of Cu(In, Ga)Se₂ thin-film

solar cells – an update, *Advances in Solid State Physics* 44 (2004) 27–38. doi:10.1007/b95888.